

A&A manuscript no.  
(will be inserted by hand later)

Your thesaurus codes are:  
02 (12.03.3; 11.03.1; 13.25.3)

# The Baryon Content of Groups and Clusters of Galaxies

H. Roussel<sup>1</sup>, R. Sadat<sup>2</sup>, A. Blanchard<sup>2,3</sup>

<sup>1</sup> DAPNIA/Service d'Astrophysique, CEA/Saclay, 91191 Gif-sur-Yvette cedex, France

<sup>2</sup> Observatoire Midi-Pyrénées, 14 Av. Edouard Belin, 31 400, Toulouse, France

<sup>3</sup> Observatoire Astronomique, 11, rue de l'Université, 67000 Strasbourg, France

Received \_\_\_\_\_ ; accepted \_\_\_\_\_

**Abstract.** We have analyzed the properties of a sample of 33 groups and clusters of galaxies for which both optical and X-ray data were available in the literature. This sample was built to examine the baryon content and to check for trends over a decade in temperature down to 1 keV.

We examine the relative contribution of galaxies and ICM to baryons in clusters through the gas-to-stellar mass ratio ( $M_{gas}/M_*$ ). We find that the typical stellar contribution to the baryonic mass is between 5 and 20%, at the virial radius. The ratio ( $M_{gas}/M_*$ ) is found to be roughly independent of temperature. Therefore, we do not confirm the trend of increasing gas-to-stellar mass ratio with increasing temperature as previously claimed.

We also determine the absolute values and the distribution of the baryon fraction with the density contrast  $\delta$  with respect to the critical density. Virial masses are estimated from two different mass estimators: one based on the isothermal hydrostatic equation (IHE), the other based on scaling law models (SLM), the calibration being taken from numerical simulations. Comparing the two methods, we find that SLM lead to less dispersed baryon fractions over all density contrasts and that the derived mean absolute values are significantly lower than IHE mean values: at  $\delta = 500$ , the baryon fractions (gas fractions) are 11.5–13.4 % (10.3–12 %) and  $\sim 20\%$  (17 %) respectively. We show that this is not due to the uncertainties on the outer slope  $\beta$  of the gas density profile but is rather indicating that IHE masses are less reliable. Examining the shape of the baryon fraction profiles we find that cluster baryon fractions estimated from SLM follow a scaling law. Moreover, we do not find any strong evidence of increasing baryon (gas) fraction with temperature: hotter clusters do not have a higher baryon fraction than colder ones, neither do we find the slope  $\beta$  to increase with temperature.

The absence of clear trends between  $f_b$  and  $M_{gas}/M_*$  with temperature is consistent with the similarity of baryon fraction profiles and suggests that non-gravitational processes such as galaxy feedback, necessary to explain the observed luminosity–temperature rela-

tionship, do not play a dominant rôle in heating the intra-cluster gas on the virial scale.

## 1. Introduction

Clusters of galaxies are fascinating objects because their observations can in principle allow one to constrain the parameters of the standard cosmological model. In particular, they are widely used as indicators of the mean matter density of the universe. Galaxy clusters have been shown to harbour very large quantities of dark matter since the pioneering work of Zwicky (1933), but its exact quantity, its spatial distribution and above all its very nature are still awaiting answers.

Clusters are the most massive objects for which both the luminous baryonic mass (consisting of the X-ray emitting intracluster gas and the visible part of galaxies) and the total gravitating mass can be estimated. Most often, the assumption of isothermal hydrostatic equilibrium (IHE) of the intra-cluster gas within the dark matter potential well is adopted to derive the total mass of clusters from X-ray observations, although many clusters exhibit obvious substructures, both in the galaxy distribution and in the X-ray emission morphology.

Beyond the classical  $M/L$  ratio, clusters are at the center of new cosmological tests of the mean density, which are different in spirit and which are more global. Partly because of this new perspective, general observational properties of clusters have been investigated in detail in recent years. These studies were triggered by analytical arguments as well as numerical simulations which indicated that clusters might have similar properties in their structure. A first means of determining the mean density from clusters is to use their abundance as well as their relative evolution with redshift (Oukbir & Blanchard 1992 ; Bartlett 1997). A further important property of clusters is that their baryon fraction  $f_b$  is expected to be identical (White et al. 1993), reflecting the universal baryonic content of the universe. As primordial nucleosynthesis calculations provide very strong constraints on the value of the

baryonic density parameter  $\Omega_b$ , determining the baryonic fraction in galaxy clusters allows to derive the matter density parameter  $\Omega_0 = \Omega_b / f_b$ . This surmise, when applied to a set of clusters, leads to a high mean baryon fraction  $f_b$ , of the order of  $20 h_{50}^{-3/2}\%$  (David et al. 1995, hereafter D95; White & Fabian 1995; Cirimele et al. 1997; Evrard 1997). Consequently, the critical value  $\Omega_0 = 1$  is disfavored (as the primordial nucleosynthesis is indicative of  $\Omega_b = 0.0776 h_{50}^{-2} \eta_{10}/5.3 \pm 7\%$ , one obtains  $\Omega_0 \sim 0.4$ ). White et al. (1993) have reviewed this critical issue in the case of the Coma cluster.

Some caution is necessary though, since there exists an appreciable dispersion in the range of published baryon fractions. This scatter may be due to intrinsic dispersion in baryon fractions of different clusters. If real, it is important to understand the origin of such a scatter. However, Evrard (1997) did not find any convincing evidence for a significant variation in the baryon fraction from cluster to cluster. Such a result is in contrast with Loewenstein & Mushotzky (1996) and D95. These latter authors, from their study of ROSAT PSPC observations of a sample of groups and clusters of galaxies, have found a correlation between the gas fraction and the gas temperature, breaking the simplest self-similar picture (the different conclusion of Evrard could be due to the limited range of temperatures he used). A possible explanation for such variations, if real, could in principle be the development of a segregation between baryons and dark matter occurring during the cluster collapse, operating more efficiently in massive clusters. However, this mechanism has been shown by White et al. (1993) to be insufficient to significantly enhance the baryon fraction and it is therefore unlikely that such a phenomenon could lead to a substantial scatter in baryon fractions. Another possibility is that in poor clusters and groups, a part of the gas has been swept away in the shallow dark matter potential well by galactic winds, being thus less concentrated than in massive clusters. This scenario would also be consistent with the claim that the gas to stellar mass ratio increases monotonically with the temperature of the cluster (David et al. 1990, hereafter D90). Finally, a further possibility is that mass estimates are not accurate and that a systematic bias exists with temperature. In any case, D95 derived this correlation from a very reduced set of objects (7 clusters and 4 groups) and it would deserve further investigation based on a larger sample.

As a consequence, it was one of our aims to address these questions with improved statistics. Moreover, in the baryon problem, the reliability of mass estimates is rather crucial and assumptions such as equilibrium and isothermality may introduce systematic differences in the results that we wish to examine in detail. The validity of mass estimates has been questioned by Balland & Blanchard (1997). We have therefore taken the opportunity of this study to perform a comparison between the standard mass estimate based on the IHE  $\beta$ -model and an alternative

method derived from scaling arguments and numerical simulations including gas physics (see section 3.3), hereafter called the scaling law model (SLM).

In this paper, we present an analysis of a sample of 26 galaxy clusters and 7 groups taken from the literature. We required that optical data were available for our objects and searched for a precise information on the galaxy spatial distribution and luminosity function, on the X-ray temperature and on the gas density profile, in order to be able to build up the density and mass profiles for galaxies, gas and dark matter. This allows to compute properly the baryon fraction rather than only the gas fraction as is often done. This is especially important for low mass objects, in which the stellar component is generally believed to be relatively more important. Our sample comprises clusters with temperature from 1 to 14 keV, and therefore allows us to investigate several interesting quantities beyond gas and baryon fraction, like the mass to light ratio and the ratio of galaxy baryonic mass to gas mass (possibly providing important constraints on galaxy formation), over a wide range of temperatures. All the data used here come from the literature, with the exception of Abell 665, for which we have analysed an archival ROSAT image to obtain the gas density profile. In fact, this cluster has already been studied from Einstein data by two teams (Durret et al. 1994; Hughes & Tanaka 1992), finding in each case a surprisingly very high gas fraction (respectively  $\simeq 50\%$  and  $33\%$ ). We will see this cluster provides a striking example of the differences in mass determinations.

The sample is presented in section 2. The methods to compute the various quantities for each cluster in the sample is presented in section 3 and the results are presented in Section 4. In section 5, we examine the trend with temperature for several quantities.

In all the present study, we assumed a  $H_0 = 50 \text{ km s}^{-1} \text{ Mpc}^{-1}$  and  $q_0 = 0.5$  cosmology.

## 2. The sample

We looked in the literature for objects studied thoroughly enough to allow us to compute the baryonic mass in galaxies, the mass in gas and in dark matter at any radius. This is quite not a refinement, since both the baryon fraction and the galaxy to gas mass ratio can vary very rapidly with radius, as will be seen in the next section. We therefore needed detailed information, which drastically reduced the possible number of objects that could be included in the sample. When a same object was studied by several teams, we applied straightforward selection criteria : for spatial X-ray data, for instance, we systematically prefer ROSAT observations, because of its improved spatial resolution and sensitivity, whereas for X-ray temperatures, Ginga and ASCA satellites were preferred to Einstein MPC, most of which come from the catalogue of David et al. (1993). **Recently, it has been noticed that cluster luminosities and temperatures**

might change noticeably when the central cooling flow emission is removed (Markevitch 1998 ; Arnaud & Evrard 1999). It is not clear which temperatures are to be used (especially when using a mass-temperature relationship derived from numerical simulations). In order to keep our sample as homogenous as possible, we did not use cooling flow-corrected temperatures which are not always available. Furthermore Markevitch (1998) found that temperatures corrected for central emission are in the mean 3% larger, which will be of weak consequence in our average quantities. However, our treatment of the uncertainties on temperatures leads to large error bars when a large dispersion in measured temperatures exists (see Table 1), as for instance in the presence of strong cooling flow.

In some cases, optical data may be very uncertain because of projection effects and magnitude limitations, especially for groups whose galaxy membership is sometimes tricky to establish. However, we tried to identify objects for which data are reasonably reliable and we derived mean dynamical quantities for this sub-sample as well. Finally, it must be emphasised that the X-ray limiting radius at which baryon fractions are estimated is a crucial parameter, since both the galactic mass derived from a King profile and the X-ray gas mass given by the Hubble-King model diverge respectively for  $\epsilon \leq 1$  and  $\beta \leq 1$  (the definition is given in 3), requiring that they be truncated. It is also important that the baryon fractions of different clusters be computed at an equivalent scale in order to test the scaling hypothesis and if statistical conclusions are to be brought out from them, *i.e.* that we use the radius containing the same overdensity, while information is actually available only up to the X-ray limiting radius  $R_{X \text{ lim}}$  which primarily depends on the characteristics of the observations (detector sensitivity, integration time...).

X-ray and optical data are summarised in Tables 1 and 2, using a Hubble constant  $h_{50} = 1$ . Notes on clusters which required a special treatment due to an incompleteness of data can be found at the end. Optical luminosities are given in the blue band. When the blue luminosity was not available, we used the following colors, corresponding to standard values for elliptical galaxies : B-V = 0.97, V-F = 0.76, r-F = 0.58 (Schneider et al. 1983) and R = F (Lugger 1989).

### 2.1. The case of Abell 665

This cluster is one for which large baryon fraction estimates have been published in the literature. As these are surprisingly high, we have found interesting to re-analyse this cluster using a ROSAT archival image and the calibration routines of Snowden et al. (1994). We found that

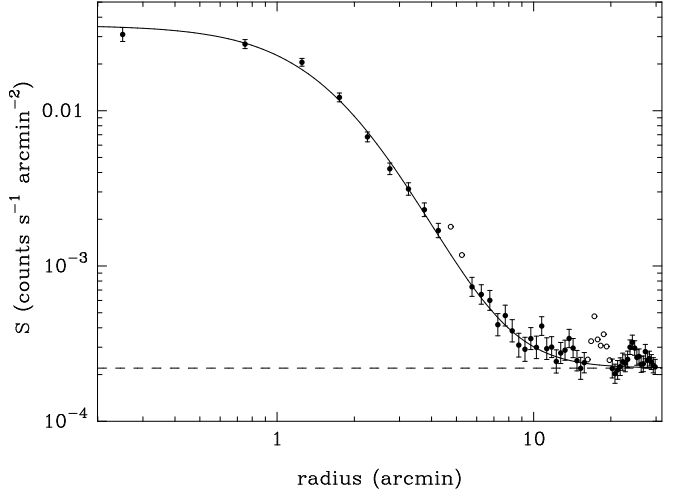


**Fig. 1.** Surface brightness profile of the intracluster gas in A665, in the ROSAT bands R4 to R7 (0.44 to 2 keV). Points represented by an empty circle have been excluded from the fit because at these radii some background or foreground X-ray sources appear in the map. The dashed line is the fitted background level.

the gas surface brightness profile is well fitted by a Hubble-King law, and the X-ray emission can be traced out to a very large radius. The background level, which has been fitted together with the other parameters, is estimated with comfortable confidence. Spherical symmetry was assumed to derive the surface brightness profile in 0.5 arcmin wide annuli, although the X-ray map shows significant departure from sphericity ; however, the effect of ellipticity on derived masses is known to be negligible (Buote & Canizares 1996). The central electron volume density  $n_{e0}$  was computed by matching the theoretical count rate with the  $0.547 \text{ counts s}^{-1}$  collected within a 30 arcmin radius (after subtraction of the background), which amounts to solving:

$$n_{e0}^2 \alpha_E D T^{-\frac{1}{2}} \int_{E_{\min}}^{E_{\max}} \frac{g(T, E) e^{-\frac{E}{kT}} e^{-\sigma(E) N_H} A(E)}{E} dE \int_0^{\theta_{\max}} \left(1 + \left(\frac{\theta}{\theta_c}\right)^2\right)^{-3\beta} \theta^2 d\theta = 2\pi S_0 \int_0^{\theta_{\max}} \left(1 + \left(\frac{\theta}{\theta_c}\right)^2\right)^{(-3\beta + \frac{1}{2})} \theta d\theta, \quad (1)$$

with  $\alpha_E = 1.02 \cdot 10^{-17} \text{ SI}$  and the angular distance  $D \simeq 812 \text{ Mpc}$ , and where  $A(E)$  stands for the energy dependence of the transmission efficiency. The results of this analysis are the following (for the bands R4 to R7 of ROSAT) :  $\beta = 0.763 \pm 0.023$ ,  $\theta_c = (112 \pm 5) \text{ arcsec}$  (which corresponds to 0.44 Mpc at the distance of A665),  $n_{e0} = (2.85 \pm 0.38) \cdot 10^{-3} \text{ electrons cm}^{-3}$  and  $R_{X \text{ lim}} = 10 \text{ arcmin}$  ( $= 2.36 \text{ Mpc}$ ) with a central surface brightness  $S_0 = (3.53 \pm 0.26) \cdot 10^{-2} \text{ counts s}^{-1} \text{ arcmin}^{-2}$

and a background surface brightness  $b = (2.2 \pm 0.6) 10^{-4} \text{ counts s}^{-1} \text{ arcmin}^{-2}$ . We used the gas temperature and foreground absorbing hydrogen column density given by Hughes & Tanaka (1992) from their Ginga analysis, together with the formula of Mewe et al. (1986) for the Gaunt factor and that of Morrison & McCammon (1983) for the interstellar absorption cross section. At  $R_{X\text{lim}}$ , the inferred gas mass is  $M_{\text{gas}} = (2.46 \pm 0.76) 10^{14} M_{\odot}$  (at, which is similar to the values found by Durret et al. (1994) and Hughes & Tanaka (1992)). The hydrostatic mass is  $M_{\text{hydro}} = (1.60 \pm 0.24) 10^{15} M_{\odot}$ . Our mass estimate from NFW's dark matter profile, computed with the EMN normalisation (see section below) is  $M_{\text{dark}} = (1.41 \pm 0.25) 10^{15} M_{\odot}$ , and the resulting total mass is  $M_{\text{SLM}} = (1.68 \pm 0.33) 10^{15} M_{\odot}$ . The baryon fraction amounts to respectively  $(16.3 \pm 7.5)\%$  and  $(15.6 \pm 6.4)\%$ . Hence A665 is a quite ordinary rich cluster whose baryon fraction seems reasonable if compared to previous values. We have also compared our gas mass estimates for the whole sample with other published analyses and found good agreement while the main differences are on  $f_b$ , coming from the estimation of total masses as will be discussed in 5.

### 3. Analysis methods

#### 3.1. The stellar mass profile

The stellar matter content can be computed at any radius from the cluster center using the projected number density profile of galaxies, their luminosity function and a mass to light ratio for the stellar population calibrated on the observation of nearby galaxies. Most often, the density profile is fitted by the common King form :

$$\sigma_{\text{gal}}(r) = \sigma_0 \left(1 + \left(\frac{r}{r_c}\right)^2\right)^{-\epsilon} \quad \text{with } \epsilon = 1, \quad (2)$$

where  $r_c$  is the galactic core radius. The case  $\epsilon = 1$  is an approximation to the isothermal sphere, in which galaxies have reached their equilibrium distribution. The advantage of such a model is that the volume density is obtained by an analytical deprojection. However, de Vaucouleurs profiles, which are much steeper in the cluster core, provide a better approximation to the real distribution (Rhee & Latour 1991 ; Cirimele et al. 1997), at the same time leading to a finite total number of galaxies :

$$\sigma_{\text{gal}}(r) = \sigma_0 \exp\left(-\left(\frac{r}{r_v}\right)^\gamma\right). \quad (3)$$

This sort of profile was deprojected using the formula :

$$\nu(r) = -\frac{1}{2\pi r} \frac{d}{dr} \int_{r^2}^{+\infty} \frac{\sigma(p)}{\sqrt{p^2 - r^2}} dp^2, \quad (4)$$

$p$  being the projected distance to the cluster centre and  $r$  the true distance. Because this deprojection is numerically unstable, we computed it by assuming  $\sigma(p)$  to be

constant inside a grid step and then integrating analytically the denominator. The mass to light ratio applied to all clusters and groups (but the supposed fossil group RXJ 1340.6+4018 consisting of only one giant elliptical galaxy, for which we used  $M_*/L_B = 8.5 h_{50} M_{\odot}/L_{B\odot}$ ) is  $M_*/L_B = 3.2 h_{50} M_{\odot}/L_{B\odot}$ , obtained by White et al. (1993) by averaging over the Coma luminosity function the  $M_*/L$  ratio from van der Marel (1991) given as a function of luminosity for bright ellipticals. Then, using the Schechter luminosity function :

$$n(L)dL = N^* \left(\frac{L}{L^*}\right)^{-\alpha} e^{-\frac{L}{L^*}} d\left(\frac{L}{L^*}\right), \quad (5)$$

the luminosity emitted by a shell of thickness  $dr$  and situated at the radius  $r$  writes as :

$$dL(r) = L_{\text{tot}} \times (4\pi r^2 \nu_{\text{gal}}(r) dr) / N(> L_{\text{lim}})$$

where  $N(> L) = N^* \Gamma(1 - \alpha, L/L^*)$  is the total number of galaxies brighter than  $L$ ,  $L_{\text{lim}}$  being the limiting luminosity of the observations, and  $L_{\text{tot}} = N^* L^* \Gamma(2 - \alpha)$ . The stellar mass enclosed in a sphere of radius  $R$  can eventually be written as :

$$M_*(R) = \frac{M_*}{L} \frac{L^* \Gamma(2 - \alpha)}{\Gamma(1 - \alpha, \frac{L_{\text{lim}}}{L^*})} \int_0^R 4\pi r^2 \nu_{\text{gal}}(r) dr. \quad (6)$$

When no parameters for the luminosity function were found in the literature, we adopted the standard ones (Schechter 1975) :  $\alpha = 1.25$  and  $M_V^* = -21.9 + 5 \log h_{50}$ .

As a few clusters observed in X-rays do not have any available spatial galaxy distribution (or with too poor statistics), but only either a luminosity profile or even several total luminosities given at different radii, we then assumed a King profile and fitted the few points by the resulting integrated luminosity profile :

$$L(< R) = L_0 \left[ \ln \left( \frac{R}{r_c} + \left(1 + \left(\frac{R}{r_c}\right)^2\right)^{\frac{1}{2}} \right) - \frac{R}{r_c} \left(1 + \left(\frac{R}{r_c}\right)^2\right)^{-\frac{1}{2}} \right] \quad (7)$$

by varying simultaneously  $L_0$  and  $r_c$ . In addition to those cases, RXJ 1340.6+4018 was treated in a special way : we deprojected a de Vaucouleurs luminosity profile (Ponman et al. 1994).

#### 3.2. The X-ray gas mass profile

**In their pioneering work, Cavaliere & Fusco-Femiano (1976) have shown under the isothermality assumption, that the X-ray gas profile is described by:**

$$\rho_{\text{gas}}(r) = \rho_0 \left(1 + \left(\frac{r}{r_{\text{cx}}}\right)^2\right)^{-\frac{3}{2}\beta} \quad (8)$$

which translates to the observed X-ray surface brightness with the following simple analytical form (the so-called  $\beta$ -model):

$$S(\theta) = S_0 \left(1 + \left(\frac{\theta}{\theta_c}\right)^2\right)^{-3\beta + \frac{1}{2}}, \quad (9)$$

the slope  $\beta$  and the core radius  $r_{cX}$ , which are interdependent in their adjustment to the surface brightness, being generally found to range between 0.5 and 0.8 and between 100 and 400 kpc respectively. Very often, central regions of clusters have to be excluded from the fit, due to cooling flows resulting in an emission excess. The gas mass can be inferred accurately from the knowledge of  $S_0$ ,  $\beta$  and  $\theta_c$ . Uncertainties in the gas mass are small in general, as long as it is computed inside a radius at which the emission is detected. The relationship between the electron number density and the gas mass density used here is  $\rho_0 = 1.136 m_p n_{e0}$  (assuming a helium mass fraction of 24% and neglecting metals).

### 3.3. The binding mass profile

Mass estimation is certainly the most critical aspect of recent studies of the baryonic fraction in clusters. Clarifying this issue is one important aspect of this paper. We derived the gravitational mass in two ways :

- *The hydrostatic isothermal  $\beta$ -model :*

First, we used the standard IHE assumption which, using spherical symmetry, translates into the mass profile :

$$\begin{aligned} M_{\text{tot}}(r) &= -\frac{k}{G\mu m_p} T_X r \frac{d \ln \rho_{\text{gas}}(r)}{d \ln r} \\ &= \frac{3k}{G\mu m_p} \beta T_X r \left(1 + \left(\frac{r}{r_{cX}}\right)^{-2}\right)^{-1}. \end{aligned} \quad (10)$$

The total mass thus depends linearly on both  $\beta$  and  $T_X$ . Hence, if the slope of the gas density is poorly determined (and this is the case if the instrumental sensitivity is too low to achieve a good signal to noise ratio in the outer parts of the cluster), it will have a drastic influence on the derived mass. This mass profile results in the density profile :

$$\rho_{\text{tot}}(r) \propto \frac{1}{r^2} \left[ 3 \left(1 + \left(\frac{r}{r_{cX}}\right)^{-2}\right)^{-1} - 2 \left(1 + \left(\frac{r}{r_{cX}}\right)^{-2}\right)^{-2} \right] \quad (11)$$

and in a flat density at the cluster centre.

**The isothermality assumption can be questioned since Markevitch et al. (1998) found evidence for strong temperature gradients in clusters, which may lead to IHE mass estimates smaller by 30% (Markevitch 1998). Although the reality of these gradients has recently been questioned (Irwin et al., 1999; White 2000).**

- *The universal density profile :*

An alternative approach is to use the universal dark matter density profile of Navarro et al. (1995, hereafter NFW) derived from their numerical simulations :

$$\frac{\rho_{\text{dark}}(r)}{\rho_c} = 1500 \frac{r_{200}^3}{r (5r + r_{200})^2} \quad (12)$$

where  $r_{200}$  stands for the radius from the cluster center where the mean enclosed overdensity equals 200 (this is the virial radius) and  $\rho_c$  is the critical density. It varies as  $r^{-1}$  near the centre, being thus much steeper than in the hydrostatic case ; NFW claim this behaviour fits their high resolution simulations better than a flat profile. Furthermore, contrary to the  $\beta$ -model, the dark matter density profile obtained by NFW is independent on the shape of the gas density distribution. This will introduce a further difference. The normalisation of the scaling laws ensures a relationship between temperature, virial radius and virial mass. Here, this normalisation is taken from numerical simulations. Different values have been published in the literature (see for instance Evrard, 1997 ; Evrard et al., 1996, EMN hereafter ; Pen, 1998 ; Bryan and Norman, 1998, BN hereafter). Frenk et al. (1999) investigated the formation of the same cluster with various hydrodynamical numerical simulations. They found a small dispersion in the mass-temperature relation : the rms scatter  $\sigma$  is found to be of  $\approx 5\%$ , EMN and BN lying at the edges of the values found, representing a  $4 \sigma$  difference. EMN provide a scaling law between  $r_{500}$  and  $T_X$  :

$$r_{500} = 2.48 \left(\frac{T_X}{10 \text{ keV}}\right)^{\frac{1}{2}} h_{50}^{-1} (1+z)^{-\frac{1}{2}} \text{ Mpc} \quad (13)$$

(in terms of comoving radius) which was used here to compute  $r_{200}$ , writing :

$$\begin{aligned} \delta(r_{500}) = 500 &= \left(\frac{4}{3} \pi r_{500}^3\right)^{-1} \int_0^{r_{500}} 4\pi r^2 \frac{\rho(r)}{\rho_c} dr \\ &= 180f X^{-3} \left[ \ln(1+5X) - \frac{5X}{1+5X} \right] \end{aligned} \quad (14)$$

with  $X = r_{500}/r_{200}$ , where  $f = 1739/1500$  is a corrective factor to transform dark matter mass into total mass, so that  $\delta(r_{200})$  is really equal to 200. Solving this equation gives  $X = 0.66$ . The relation at  $z = 0$  between virial mass and temperature can then be written as :

$$T_X = 4.73 M_{15}(r_{200})^{\frac{2}{3}} \text{ keV}. \quad (15)$$

BN did provide the following constant of normalisation :

$$T_X = 3.84 M_{15}(r_{200})^{\frac{2}{3}} \text{ keV}. \quad (16)$$

This difference is quite significant : it does correspond to a virial mass 40% higher. Using this normalisation will obviously significantly change the inferred gas fraction.

## 4. Results

### 4.1. Distribution of the various components

The results from our analysis for each cluster in our sample are summarised in Tables 3 to 6 : in Table 3 and Table 5 mass estimates at  $r_{200}$  are derived from the SLM with the  $T_X - M_V$  calibrations respectively given by EMN and BN (used to compute  $r_{200}$ ). In Table 4 and Table 6 are summarised mean dynamical quantities over the sample at three different overdensities,  $r_{200}$ ,  $r_{500}$  and  $r_{2000}$ . The same quantities are also given with mass estimates from the IHE model.

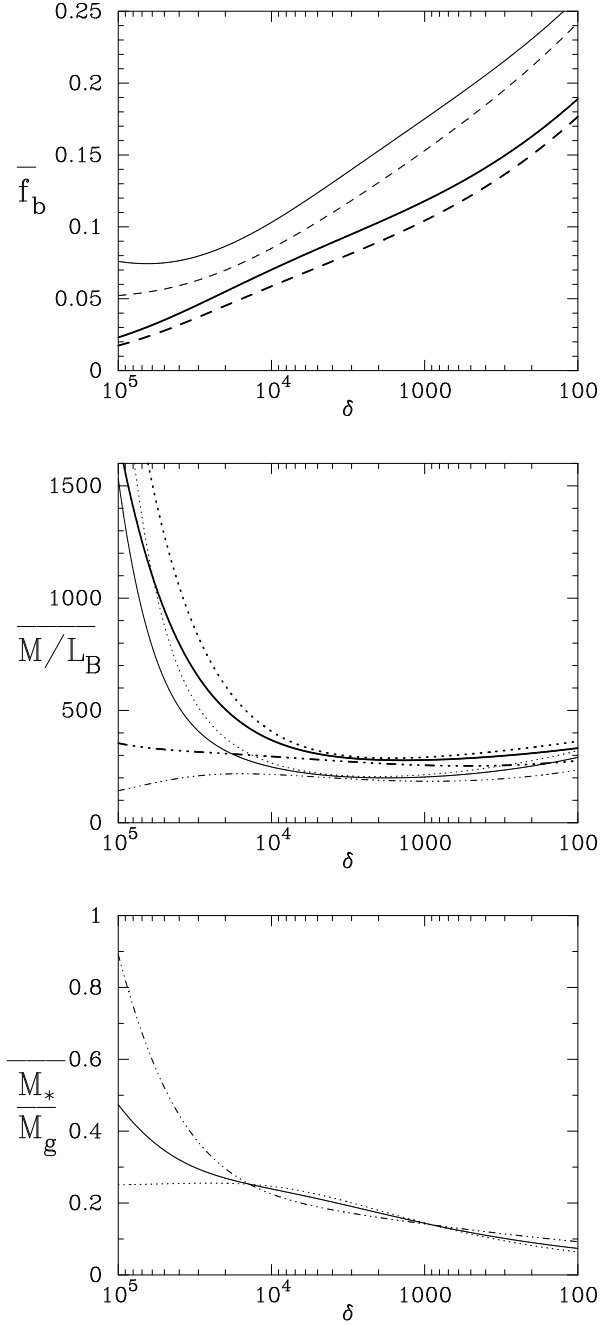


**Fig. 4.** Average profiles for all clusters (groups included) with the most reliable data. Top : baryon fraction (continuous lines) and gas fraction (dashes) in the case of SLM mass estimates with the EMN normalisation (thick lines) and hydrostatic masses (thin lines). Middle : mass to luminosity ratio for the whole sample (continuous lines), for King galaxy profiles only (dots) and for de Vaucouleurs profiles only (dash-dots), with the same convention as previously. Bottom : stellar mass to gas mass ratio, with the same line styles as for  $M/L_B$ .

#### 4.1.1. The binding mass

Mass profiles of the various components for a few clusters are displayed in figure 2, together with mass ratio profiles (right side). Figure 3 shows baryon and gas fraction profiles for the whole sample. Quantities are plotted against the mean enclosed contrast density, which is the natural variable in the scaling model. A clear feature arising from Figure 2 concerns the different behaviours of hydrostatic masses and total masses deduced from NFW's dark matter profile, normalised by the EMN  $T_X - M_V$  relationship : NFW profiles are more centrally concentrated, as could be foreseen from Equ.11 and 12, a property which is in agreement with the density profile of clusters inferred from lensing (Hammer 1991, Tyson et al. 1990). In the outer part, when the contrast density is smaller than a few  $10^4$ , the shapes of the density profiles are quite similar, although some difference in the amplitude exists. In fact, profiles calibrated from the EMN  $T_X - M_V$  relation tend to be systematically more massive than with the isothermal hydrostatic model, with a significant dispersion. The last column of Tables 3 and 5 gives the ratio between masses computed with both methods. The mean of masses estimated by the IHE  $\beta$ -model is significantly smaller than SLM masses (at  $R_{X\text{lim}}$ ):  $M_{IHE}/M_{SLM} = 0.80 \pm 0.03$  with EMN normalisation, and  $M_{IHE}/M_{SLM} = 0.67 \pm 0.026$  with BN normalisation. Clearly, such a difference will translate into the baryon fraction estimates.

#### 4.1.2. The X-ray gas

Second, the distribution of gas is more spread out than that of dark matter, which results in steadily rising baryon fractions with radius (Fig. 4), as was already pointed out by numerous teams, among which Durret et al. (1994) and D95. NFW also recover this trend in their simulations. This fact makes the choice of the limiting radius an important matter. In particular, extrapolating masses to the virial radius (which is reached by the gas emission in only five clusters among our sample) could be very unsafe, especially for cool clusters, the gas of the most extended of our objects with  $T_X \leq 5$  keV being detected only out to  $\delta = 500$ .

#### 4.1.3. Mass to light ratio

The derived mean mass to blue luminosity ratio is shown in figure 4. As it can be seen,  $M/L_B$  remains remarkably constant from  $\delta \simeq 5000$  to the outer parts of clusters, in the case of total masses derived from SLM as well as that of hydrostatic masses. Thus, the widely spread assumption that light traces mass is confirmed, at least at  $r \geq r_c$ . The influence of the choice of de Vaucouleurs galaxy density profiles as compared to King profiles is also clearly highlighted. In fact, in the core, dark matter is normally much more concentrated than galaxies,

but using a de Vaucouleurs distribution, it turns out that the concentration factor is considerably lowered and even reversed in the case of hydrostatic masses. Mixing the two shapes of galaxy distribution in our sample, the result is an intermediate behaviour.

#### 4.2. The baryon fraction

We find that inside a same object, the gas and baryon fractions increase from the center to outer shells (Fig. 3 and Fig. 4), reflecting the fact that the distribution of gas is flatter than that of dark matter, a trend similar to what is found by D95. Secondly, an interesting feature can be noted from figure 3: the baryon fraction profiles versus density contrast are remarkably similar and seem to follow a regular behaviour, consistent with **an universal baryon fraction shape**, even in the central part (although with a larger dispersion). This behaviour appears more clearly when one is using the SLM model. This result is consistent with the baryon fraction following a scaling law as it has been already found for the emissivity profiles (Neumann & Arnaud, 1999) **and gas profiles (Vikhlinin et al., 1999)**. Thirdly, the comparison of the graphs of figure 3 shows that the baryon fraction  $f_{SLM}$  estimated from the NFW profile normalised with the EMN  $T_X - M_V$  relationship is less dispersed at all contrast densities. This effect is asymmetric : the high baryon fractions  $f_{IHE}$  found with the IHE method disappear. The fact that  $f_{SLM}$  appears less dispersed has already been found by Evrard (1997) and Arnaud & Evrard (1999). However, our work indicates that this feature exists at any radius. We also plot in Figure 5 the histograms of baryon fractions as derived from both the IHE and SLM methods at the virial radius  $r_{200}$  but also at  $r_{2000}$  chosen because each object of the sample is detected in X-rays at least out to  $\delta \sim 2000$ . The comparison of the two indeed provides an evidence for SLM masses to lead to more tightened baryon fractions than hydrostatic masses. **At the virial radius, we found that the intrinsic dispersion is 50% with the IHE and 20% with SLM.** This bears an important consequence for the interpretation of mass estimates as well as the interpretation of the baryon fraction. Clearly the fact that the baryon fraction is less dispersed in the SLM even in the central regions shows that this mass estimate is safer and that the IHE method provides less accurate mass estimates even in the central region where hydrostatic equilibrium is expected to hold.

##### 4.2.1. Stellar to gas mass ratio $M_*/M_{gas}$

Also shown in figure 4 is the mean  $M_*/M_{gas}$  ratio as a function of overdensity, slowly going down after the central part. The galaxy density is indeed steeper than that of gas, decreasing in  $r^{-3}$  with  $\epsilon = 1$  instead of  $r^{-2}$  for a typical value of  $\beta = 0.66$ , and the situation is even worse when a de Vaucouleurs profile is used for the galaxy distribution.

Again, the latter contributes in a large amount to the steep decrease in the central regions, whereas there the ratio is flat with King profiles.

#### 4.3. Numerical results

Average numerical results are presented in Tables 4 and 6. It is found that the mean baryon fraction using the SLM with the  $T_X - M_V$  normalization of EMN is 13.4% and the gas fraction 11.5% at  $r_{500}$  to be compared with hydrostatic results : respectively 19.2 and 17.0%. As expected, the two methods of mass estimation lead to different baryon (gas) fractions. This difference is not negligible ( $\approx 40\%$ ) and is mainly due as already noted, to the difference between the IHE mass and the SLM mass. The IHE mass can be 50 to 60% lower with respect to the SLM mass (this is the case, for instance, of the groups HCG 62, NGC 2300 and NGC 4261). This difference between  $f_b^{SLM}$  and  $f_b^{IHE}$ , increases when using the  $T_X - M_V$  normalization of BN (the mean baryon fraction being then 11.5 and the mean gas fraction 10.3%). Cirimele et al. (1997) found  $f_b = 23\%$  for their 12 clusters included in our sample (and 20% excluding A76), instead of our result of 19% (and 16%) using their parameters and the same hydrostatic  $\beta$ -model and their limiting radius (they choose a uniform  $R_{Xlim} = 1.5$  Mpc ) and of 13% using the SLM method. The disagreement is due to the adopted stellar mass to light ratio ( $M/L_B = 10.7$  instead of our 3.2 value). From the results of D95, it comes out that their 7 clusters also have a mean baryon fraction of  $f_b \approx 23\%$ . Thus, this is a confirmation of the divergence between hydrostatic  $\beta$ -model mass estimates and SLM's masses. From a sample of 26 clusters among which 7 hot and 3 cool clusters are in our sample, Arnaud & Evrard (1999) have made a similar analysis and derived in the frame of simulation-calibrated virial masses a mean gas fraction at  $\delta = 500$  of  $\simeq 14\%$  in rough agreement with our value of 12%. If the comparison is restricted to hot cluster subsamples, the agreement is as good (they found 16 % to be compared with our 14%), and also at  $r_{200}$ . A somewhat higher gas fraction ( $f_g \approx 17\%$ ) has been obtained recently by Mohr et al. (1999), as compared to ours, which is probably due to the difference in the normalization of the  $T_X - M_V$  relationship.

Another output from the present study is the mean total mass to blue luminosity ratio  $M/L_B \simeq 270$  at  $r_{2000}$  (the hydrostatic assumption leading to  $M/L_B \simeq 200$ ), groups and clusters of all temperatures put together. However, when looking in more detail at the three classes of groups (with  $T_X \leq 2$  keV), cool clusters ( $T_X \leq 5$  keV) and hot clusters,  $M/L_B$  (at  $r_{2000}$ ) goes from 200 to 270 and 340 respectively, with similar statistics (7 groups, 10 cool clusters and 8 hot clusters). Hence, we disagree with D95 who claim that the mass to light ratio is roughly constant from groups to rich clusters (using the group NGC 5044 which also belongs to our sample with  $M/L_B \simeq 160$ , 2

cool clusters and 4 hot clusters, 3 of which are also in common with ours). It is worth noticing that 2 of the 3 clusters in common have a low  $M/L_B$  in our analysis : 150 for A85 and 170 for A2063. This conclusion holds whatever the limiting radius : there is a factor of 1.7, 1.9 and 1.9 respectively between groups and hot clusters when examining  $M/L_B$  out to  $r_{2000}$ ,  $r_{500}$  or  $r_{200}$ .

As to the mean gas to stellar mass ratio  $M_{\text{gas}}/M_*$ , its values are summarized in Tables 4 and 6. We have computed this quantity to estimate the stellar contribution to the baryon fraction and to investigate any correlation with temperature, which will be discussed in the next section. Let us simply mention that our value for groups at  $r_{2000}$  is in good agreement with the mean value  $\simeq 5$  of Dell’Antonio et al. (1995) for 4 poor clusters, after correcting for the different  $M_*/L$  they have used.

## 5. Correlations of the baryon population properties with temperature

In order to properly understand the baryon fraction in clusters it is necessary to understand what are the relative contribution of the gas and stellar components. Several previous studies found that the stellar component is more dominant in low temperature systems, the lower gas content of small clusters being possibly due to feedback processes. Our sample, being large and covering temperatures from 1 to 14 keV, allows us to study these questions in detail.

### 5.1. The $M_{\text{gas}}/M_* - T_X$ correlation

In this section, we examine a possible correlation between the X-ray gas temperature and the ratio of gas mass to stellar mass,  $M_{\text{gas}}/M_*$ , at various radii. A strong correlation has been previously found by D90: from the analysis of twelve groups and clusters with temperatures ranging from 1 to 9 keV, D90 found that this ratio varies by more than a factor of five from groups to rich clusters. An increase of  $M_{\text{gas}}/M_*$  with cluster richness has also been reported by Arnaud et al. (1992).

This trend has been interpreted as due to the galaxy formation being less efficient in hot clusters than in colder systems. D90 suggest that the scenario for structure formation of hierarchical clustering, in which large structures form after little ones by successive mergers, is adequate to explain their result : in fact, as mergers go on, the intra-cluster gas is progressively heated by shocks to higher and higher temperatures, as the size of the structures involved increases ; the higher  $T_X$ , the more difficult it becomes for the gas to collapse and to form new galaxies. Hence, after some time, further galaxy formation would be prevented in hot clusters, producing an anti-bias.

In figure 6 we have plotted  $M_{\text{gas}}/M_*$  against temperature at the radii  $r_{2000}$  and  $r_{200}$ . As can be seen, mean figures for groups, cool clusters and hot clusters seem to

show the sequence observed by D90, but in a less pronounced way: we find that cool clusters have  $M_{\text{gas}}/M_*$  which is  $\sim 3$  times smaller than for hotter ones instead of a factor of  $\geq 5$  in D90. Moreover, this apparent sequence weakens when plotted at  $r_{200}$ :  $M_{\text{gas}}/M_*$  is only twice smaller for groups than for hot clusters.

It should be kept in mind that in figure 6, we adopted a constant galactic mass to luminosity ratio for clusters and groups, whereas it is expected to be lower for late type galaxies than for E-S0. As morphological segregation tends to raise the fraction of early type galaxies in rich clusters, taking into account this variation of  $M_*/L$  with morphological type would in fact flatten further the observed correlation between  $M_{\text{gas}}/M_*$  and  $T_X$ , as would do taking into account the difference in galactic output from groups to clusters. We conclude that our sample does not show a strong evidence, if any, of increasing  $M_{\text{gas}}/M_*$  with  $T_X$  as previously found by D90.

### 5.2. The $f_b - T_X$ correlation

Our sample spans an unprecedented wide range of temperature, allowing to test the somewhat puzzling evidence that cool clusters have lower mean gas fraction than hot clusters. This trend has been first reported by D95 and seems to be confirmed (Arnaud & Evrard 1999). A modest increase of the gas fraction with  $T_X$  has also been reported by Mohr et al. (1999). Such a trend is unexpected in a self-similar cluster evolution,  $f_{\text{gas}}$  and  $f_b$  at a given overdensity being expected to be constant, but would be naturally explained by non gravitational processes such as galaxy feedback (for instance, early supernovae-driven galactic outflows), able to heat the intergalactic gas enough to make it expand out (Metzler & Evrard 1994, 1997; Ponman et al. 1999). This is achieved more easily in shallower potential wells like those of groups, which could even experience substantial gas expulsion, thus reducing their gas fractions. Such scenarii are necessary to explain the  $L_X - T_X$  relation (Cavaliere et al., 1997).

In order to examine this issue, we plot in figure 7 the baryon fraction versus the temperature at different radii:  $R_{Xlim}$ ,  $r_{2000}$  and  $r_{200}$ . Error bars were estimated by considering uncertainties on the temperature and on metallicity for groups. Uncertainties on X-ray emission are small and leads to tiny uncertainties on the gas mass in the observed range ( $R < R_x$ ), while in the outer part, where observations are lacking, robust estimates of the uncertainties cannot be obtained, given that these uncertainties are systematic in nature. In the case of groups, metallicity uncertainty can lead to significant uncertainties on gas mass, and was therefore taken into account. As it can be seen, we do observe no obvious trend with  $T_X$ . The data are more consistent with  $f_b$  being constant and this whatever the mass estimator used. Although a weak tendency could be seen (in the frame of SLM masses), it appears swamped in the high dispersion affecting objects of a same temper-



ature. Therefore we do not confirm the trend of increasing  $f_b$  with  $T_X$  (or size) as previously found by D95. This is a rather robust conclusion as our sample covers a wide range of temperature, from 1 to 14 keV. This result is consistent with the similarity of the baryon fraction profiles we found (Fig. 3) and the absence of trend of  $M_{\text{gas}}/M_*$  with  $T_X$  indicating that non-gravitational processes such as galactic feedback are not dominant in determining the large scale structure of the intracluster medium.

### 5.3. The $f_b - \beta$ correlation

Analysing the baryon fraction versus temperature may hide or reflect some correlation which are present among other parameters. Of special interest is to check whether a correlation with  $\beta$  exists.

We first searched for a trend between  $\beta$  and the temperature. Previous studies have shown that low temperature systems exhibit a more extended ICM distribution (low  $\beta$  values) than hotter ones (Arnaud & Evrard 1999). From figure 8 we can see that no clear trend of increasing  $\beta$  with  $T_X$  is found. Although smaller  $\beta$  are found at the cool side, this might be due to a larger dispersion in  $\beta$  for the smallest potentials. We note that our result is consistent with the recent analysis of Mohr et al. (1999).

We have also examined the way the baryon fraction varies with  $\beta$  (Fig. 8). The baryon fraction derived from the hydrostatic  $\beta$  model,  $f_b^{\text{IHE}}$ , does not vary with  $\beta$  in an obvious way: if anything it decreases with increasing  $\beta$  (while no obvious correlation is found with  $T_X$ , see Fig. 7). Such a trend if real would be unexpected. Using the SLM mass estimates, the baryon fraction is much more constant and less dispersed, even at a fixed  $\beta$  (for  $\beta \sim 0.5 - 0.7$  the dispersion on  $f_b/\bar{f}_b$  is 0.23 with SLM estimates while it is 0.31 with the IHE). The fact that  $f_b$  is constant with  $\beta$  again differs from what one would expect if reheating would have a dominant role in redistributing the gas inside clusters.

### 5.4. Implications on mass estimates

As we have seen (section 4.2) the baryon fraction estimated with the SLM method is less dispersed than with the IHE method. This effect has been noticed previously (Evrard, 1997) and has been interpreted as due to the observational uncertainties in the estimation of  $\beta$ . The mass estimates (at some radius  $R$ ) can be written as:

$$M_1 = a_1 T R \quad (17)$$

and for the IHE model :

$$M_2 \sim a_2 \beta T R. \quad (18)$$

The fact that baryon fractions estimated with  $M_2$  are more dispersed can be understood just because of the extra dispersion introduced by  $\beta$  (EMN ; Arnaud & Evrard,

1999). For this to be due to the sole errors in the measurement of  $\beta$ , it would imply that the dispersion in the measurements dominates the intrinsic dispersion, resulting in a tight correlation between  $\beta$  and  $f_b$ , which is not obvious from Fig. 8: most clusters have a  $\beta$  in the narrow range 0.5 – 0.7, and the sample restricted to this range shows a larger dispersion for the baryon fraction computed with the IHE. Therefore, we conclude that the large dispersion observed in the baryon fractions estimated from the hydrostatic  $\beta$  model is intrinsic to the method itself leading to less reliable mass estimates, rather than to the uncertainty on  $\beta$  measurements.

## 6. Discussion and conclusions

We have analysed a sample of 33 galaxy clusters and groups covering a wide range of temperatures. For all clusters, X-ray and optical data were gathered from the literature (except for Abell 665 whose ROSAT PSPC data have been reanalysed by us). This has allowed us to investigate the structure of the various baryonic components of X-ray clusters. Mass estimates were derived from two different methods : first we have followed the standard hydrostatic isothermal equation (IHE method), secondly we have estimated the virial mass and mass profile by using the universal dark matter profile of NFW in which the virial radius is deduced from the scaling relation argument (SLM method), the normalisation constant being taken from EMN and from BN.

We find that virial masses (i.e. masses enclosed inside a fixed contrast density radius) are systematically and significantly lower when one is using the hydrostatic isothermal equation. **After this paper was submitted, we have been aware of a recent similar study by Nevalainen et al. (2000) who found that taking into account temperature profiles exacerbates this difference, as inferred masses are then smaller.** Examination of the baryon fraction versus contrast density has shown that the baryon fraction is more dispersed using the IHE. We have shown that this is not due to uncertainties on the  $\beta$  measurement but rather reflects the fact that the IHE method does not provide as reliable a mass estimate as the SLM, neither in the inner parts nor in the outer regions. Moreover the tightening of  $f_b^{\text{SLM}}$  profiles supports the idea that baryon profiles in clusters do have a rather regular structure, i.e. that gas distribution is nearly self-similar which is consistent with the recent studies by Vikhlinin et al.(1999) and by Neumann & Arnaud (1999) who found an evidence of regularity in gas density profiles. However, when plugging their mean standard density profile into the hydrostatic equation, these last authors found a mean total mass profile which is different from the NFW profile (their mass profile is lower than the one derived from numerical simulations). They have used the hydrostatic isothermal equation to estimate their total mass which probably

explains this discrepancy.

Our mean gas fraction at the virial radius  $r_{200}$ , using the SLM, is found to be in the range 12.6–14.6 % (for  $h = 0.5$ ), in rough agreement with Arnaud and Evrard (1999) when EMN normalization is used. The mean baryonic fraction is  $f_b^{SLM} \approx 13.7 - 16.4$ . It is important to emphasize that our analysis shows that a larger baryon fraction could be obtained when the sole hydrostatic equation is used, but it is reasonable to think that this is an overestimation due to the mass estimator itself. **Our analysis is consistent with an intrinsic dispersion of 20% in baryon fractions (but this could be due to some systematics), which means that our mean baryon fraction is uncertain by less than 0.01.**

As the observed luminosity-temperature does not follow the simple scaling expected from self-similarity, it is likely that non-gravitational heating such as galactic winds, additional energy input by Type II supernovae, play an important role in the physics of the X-ray gas and may result in inflating the gas distribution. Metzler & Evrard (1997) have studied this possibility and found that this is achieved more easily in low temperature clusters (shallow potential wells). The consequence of such an effect is an increasing gas fraction outwards within a cluster and a decreasing gas fraction with decreasing temperature. This effect is expected to be more pronounced in groups and cold clusters. From our sample, we do not observe such a trend of the baryon (gas) fraction with  $T_X$  whatever the method we use, suggesting that non gravitational heating is not playing a dominant role on the scale of the virial radius. In turn, we confirm that the baryon fraction apparently increases significantly from the center to outer parts of clusters.

Several previous studies have shown a clear trend of increasing  $\beta$  with  $T_X$ , while we do not find such a clear trend, neither we find a trend of  $f_b$  with  $\beta$  which is consistent with the absence of an  $f_b$ - $T_X$  correlation, although we find a slightly decreasing  $f_b^{IHE}$  (derived from the IHE method) with increasing  $\beta$ , but with a large dispersion. This result is important as it shows that the scatter in the baryon fractions derived from the IHE method is probably not due to the sole errors in the  $\beta$  measurement, but is rather due to the IHE mass estimator itself.

Our sample does not show any evidence of the strong indication highlighted by D90 that in low temperature systems, a larger fraction of baryons is present in the stellar component. Although a trend could be present in our sample, the data are certainly consistent with a stellar to gas mass ratio being constant with temperature (or mass), a further argument that non gravitational processes such as galactic winds are playing a minor role in the overall distribution of gas in clusters.

Finally, it appears that the properties of X-ray clusters are still difficult to quantify because of the lack of large homogenous samples of clusters for which both optical and

X-ray data are available. Such a situation is likely to improve with Chandra and XMM. Nevertheless, the sample we have studied reveals that clusters show important differences in the detail of the structure of their baryonic content, but that their global properties, baryonic fraction and stellar content do not show strong systematic differences with temperature.

#### Notes on individual clusters :

- A85 : Optical data for this cluster are unsafe and extend only out to 900 kpc. We used the observations of Murphy (1984) but, as the fit with an unusual galaxy density profile he performs is rather poor (and suffers from an inconsistency between  $H_0 = 50$  and  $H_0 = 60$ ), we chose to replace it with a standard King profile.
- A401 : As Buote & Canizares (1996) do not give the central electron density, we computed it with our program in the same way as for Abell 665, since both objects were observed with ROSAT PSPC, using the galactic hydrogen column density of David et al. (1993) and the count rate inside a given radius provided by Ebeling et al. (1996).
- A2029 : The same as for A401 applies.
- A2163 : Optical data for this cluster are unsafe. No galaxy distribution was available. We therefore fitted the integrated luminosity profile given in Squires et al. (1997), but it was not corrected for background galaxies and it extends only to 1.3 Mpc whereas  $R_{X\text{lim}} = 4.6$  Mpc.
- AWM7 : We used the list of galactic positions and magnitudes within  $1^\circ$  of the central cD of Beers et al. (1984) to build an integrated luminosity profile, corrected for incompleteness using their limiting magnitude and the standard Schechter luminosity function. The optical core radius was imposed to be the same as the X-ray core radius, which gives very similar results as excluding the three innermost galaxies (otherwise, the fitted core radius is too small and in fact, the King form is not a good representation of the central parts of clusters).
- Hydra A : The same procedure as for A2163 was applied, with the three points given by D90 :  $L_V/L_{V\odot} = 8.2 \cdot 10^{11}$  at 0.5 Mpc,  $1.3 \cdot 10^{12}$  at 1 Mpc and  $1.9 \cdot 10^{12}$  at 2 Mpc.
- HCG 62 : We derived an integrated number count profile from the list of galactic positions of Zabludoff & Mulchaey (1998) (using their velocity criteria to select true members) and fitted it with the function in Equ.7, assigning to each galaxy the mean luminosity derived from the limiting magnitude of the observations and the standard Schechter luminosity function. The number of galaxies contained in this “compact group” is much larger than usually assumed (45 members with  $m_B < 17$  instead of 4 in Hickson 1982).

- HCG 94 : Ebeling et al. (1995) claim this object has been misclassified and, from its X-ray emission, looks more like a poor cluster rather than a compact group. Only 7 galaxies are generally attributed to HCG 94 but we made use of the indication of Ebeling et al. that 12 more galaxies are observed within a 1 Mpc radius and at  $m_B \leq 18$ , to which we attribute a mean luminosity as for HCG 62. The fit by Equ.7 we perform relies entirely on this point (fixing the core radius at the X-ray value) since inclusion of the central galaxies would lead to a physically unacceptable core radius). Therefore, optical data for this object are unsafe.
- NGC 533 : As no central electron density is given by Mulchaey et al. (1996), we computed it from the gas mass that they obtain at a given distance. For the optical part, this is the same case as HCG 62. This group contains 36 members with  $m_B < 17$  instead of 4 in Geller & Huchra (1983).
- NGC 2300 : The same as for AWM7 applies, using magnitudes from the RC3 and excluding the two central galaxies from the fit instead of fixing the core radius.
- NGC 4261 : Since the central electron density Davis et al. (1995) give is inconsistent with their total gas mass, we computed it (this is again the same case as for A401 and A2029). We also used optical data directly from Nolthenius (1993) and applied the same method as for AWM7 with magnitudes taken from the RC3 (except we did not have to impose the core radius).
- RXJ 1340.6 has not been included in figures showing mass ratios as a function of overdensity, because it is a very peculiar case : the interior of the central giant elliptical galaxy is seen through a very large range of overdensities (at least out to  $\delta = 7000$ ).
- Several clusters have unreliable X-ray temperatures : A76, A426 (very strong cooling flow), A1377, A1775 (likely very strong cooling flow) and A2218 (steeply outwards-decreasing temperature profile).
- Error bars on gas mass for groups include an estimate of the metallicity uncertainty, which results in an uncertainty on the electron density. This effect was taken into account only for groups, because it is significant mostly in the case of low temperatures.

*Acknowledgements.* We acknowledge useful discussions with M. Arnaud, D. Neumann and J. Bartlett, and we thank V. Pislár for much appreciated help in ROSAT PSPC data reduction.

## References

- Arnaud M. & Evrard A. E., 1999, MNRAS 305, 631  
 Arnaud M., Rothenflug R., Boulade O., Vigroux L. & Vangioni-Flam E., 1992, A&A 254, 49  
 Balland C. & Blanchard A., 1997, ApJ 487, 33  
 Bartlett J. G., 1997, ASP Conf. Series 126, 365  
 Beers T. C., Geller M. J., Huchra J. P., Latham D. W. & Davis R. J., 1984, ApJ 283, 33 (B84)  
 Briel U. G., Henry J. P. & Böhringer H., 1992, A&A 259, L31 (BHB92)  
 Bryan G. L. & Norman M. L., 1998, ApJ 495, 80 (BN)  
 Buote D. A. & Canizares C. R., 1996, ApJ 457, 565 (BC96)  
 Butcher H. & Oemler A., 1978, ApJ 226, 559 (BO78)  
 Cavaliere A., Menci N. & Tozzi P., 1997, ApJ 484, L21  
 Cavaliere A. & Fusco-Femiano R., 1976, A&A 49, 137  
 Cirimele G., Nesci R. & Trèvese D., 1997, ApJ 475, 11 (CNT97)  
 Cruddace R. G., Kowalski M. P., Fritz G. G. et al., 1997, ApJ 476, 479 (CK97)  
 David L. P., Jones C. & Forman W., 1995, ApJ 445, 578 (D95)  
 David L. P., Jones C., Forman W. & Daines S., 1994, ApJ 428, 544 (D94)  
 David L. P., Slyz A., Jones C. et al., 1993, ApJ 412, 479 (D93)  
 David L. P., Arnaud K. A., Forman W. & Jones C., 1990, ApJ 356, 32 (D90)  
 Davis D. S., Mulchaey J. S., Mushotzky R. F. & Burstein D., 1996, ApJ 460, 601 (DM96)  
 Davis D. S., Mushotzky R. F., Mulchaey J. S. et al., 1995, ApJ 444, 582 (DM95)  
 Dell’Antonio I. P., Geller M. J. & Fabricant D. G., 1995, AJ 110, 502  
 Dressler A., 1978, ApJ 223, 765 (D78a)  
 Dressler A., 1978, ApJ 226, 55 (D78b)  
 Durret F., Gerbal D., Lachièze-Rey M., Lima-Neto G. & Sadat R., 1994, A&A 287, 733  
 Ebeling H., Voges W., Böhringer H. et al., 1996, MNRAS 281, 799 (EVB96)  
 Ebeling H., Mendes de Oliveira C. & White D. A., 1995, MNRAS 277, 1006 (EMW95)  
 Elbaz D., Arnaud M. & Böhringer H., 1995, A&A 293, 337 (EAB95)  
 Evrard A. E., 1997, MNRAS 292, 289  
 Evrard A. E., Metzler C. A. & Navarro J. F., 1996, ApJ 469, 494 (EMN)  
 Ferguson H. C. & Sandage A., 1990, AJ 100, 1 (FS90)  
 Ferguson H. C., 1989, AJ 98, 367 (F89)  
 Ferguson H. C. & Sandage A., 1988, AJ 96, 1520 (FS88)  
 Frenk C. S., White S. D. M. et al. 1999, ApJ 525, 554  
 Fukazawa Y., Makishima K., Tamura T. et al., 1998, PASJ 50, 187 (F98)  
 Garcia A. M., 1993, A&AS 100, 47 (G93)  
 Geller M. J. & Huchra J. P., 1983, ApJS 52, 61  
 Hammer F., 1991, ApJ 383, 66  
 Henry J. P., Briel U. G. & Nulsen P. E. J., 1993, A&A 271, 413 (HBN93)  
 Hickson P., Kindl E. & Auman J.R., 1989, ApJS 70, 687 (HKA89)  
 Hickson P., 1982, ApJ 255, 382  
 Hughes J. P. & Tanaka Y., 1992, ApJ 398, 62  
 Ikebe Y., Ezawa H., Fukazawa Y. et al., 1996, Nature 379, 427 (I96)  
 Irwin, J. A., Bregman, J. N. & Evrard, A. E. 1999, ApJ 519, 518  
 Kent S. M. & Sargent W. L. W., 1983, AJ 88, 697 (KS83)  
 Kent S. M. & Gunn J. E., 1982, AJ 87, 945 (KG92)  
 Loewenstein M. & Mushotzky R. F., 1996, ApJ 471, L83 (LM96)  
 Lugger P. M., 1989, ApJ 343, 572  
 Markevitch M., Forman W. R., Sarazin C. L. & Vikhlinin A., 1998, ApJ, 503, 77 (MF98)

- Markevitch M., 1998, *ApJ*, 504, 27
- Metzler C. A. & Evrard A. E., 1997, *ApJ* submitted, astro-ph/9710324
- Metzler C. A. & Evrard A. E., 1994, *ApJ* 437, 564
- Mewe R., Lemen J. R. & van den Oord G. H. J., 1986, *A&AS* 65, 511
- Mohr J. J., Mathiesen B. & Evrard A. E., 1999, *ApJ* 517, 627
- Mohr J. J., Geller M. J., Fabricant D. G. et al., 1996, *ApJ* 470, 724 (MG96)
- Morrisson R. & McCammon D., 1983, *ApJ* 270, 119
- Mulchaey J. S., Davis D. S., Mushotzky R. F. & Burstein D., 1996, *ApJ* 456, 80 (MD96)
- Murphy H. P., 1984, *MNRAS* 211, 637 (M84)
- Navarro J. F., Frenk C. S. & White S. D. M., 1995, *MNRAS* 275, 720 (NFW)
- Neumann D. M. & Arnaud M., 1999, *A&A* 348, 711
- Neumann D. M. & Böhringer H., 1995, *A&A* 301, 865 (NB95)
- Nevalainen J., Markevitch M. & Forman W., 2000, *ApJ* 532, 694
- Nolthenius R., 1993, *ApJS* 85, 1 (N93)
- Oegerle W. R. & Hoessel J. G., 1989, *AJ* 98, 1523 (OH89)
- Oegerle W. R., Hoessel J. G. & Jewison M. S., 1987, *AJ* 93, 519 (OHJ87)
- Oukbir J. & Blanchard A., 1992, *A&A* 262, L210
- Pen U.-L., 1998, *ApJ*, 498, 60
- Pislar V., Durret F., Gerbal D., Lima Neto G. B. & Slezak E., 1997, *A&A* 322, 53 (P97)
- Ponman T. J., Cannon D. B. & Navarro J. F., 1999, *Nature* 397, 135
- Ponman T. J., Allan D. J., Jones L. R. et al., 1994, *Nature* 369, 462
- Ponman T. J. & Bertram D., 1993, *Nature* 363, 51 (PB93)
- Rhee G. F. & Latour H. J., 1991, *A&A* 243, 38
- Schechter P., 1975, Ph.D. thesis
- Schneider D. P., Gunn J. E. & Hoessel J. G., 1983, *ApJ* 264, 337
- Snowden S. L., McCammon D., Burrows D. N. & Mendenhall J. A., 1994, *ApJ* 424, 714
- Squires G., Neumann D. M., Kaiser N. et al., 1997, *ApJ* 482, 648 (SN97)
- Squires G., Kaiser N., Babul A. et al., 1996, *ApJ* 461, 572 (SK96)
- Tamura T., Day C. S., Fukazawa Y. et al., 1996, *PASJ* 48, 671 (T96)
- Tyson J. A., Valdes F. & Wenk R. A., 1990, *ApJ* 349, L1
- van der Marel R. P., 1991, *MNRAS* 253, 710
- Vikhlinin A., Forman W. & Jones C. 1999, *ApJ*, 525, 47
- White D. A., 2000, *MNRAS* 312, 663 (W00)
- White D. A., Jones C. & Forman W., 1997, *MNRAS* 292, 419 (WJF97)
- White D. A. & Fabian A. C., 1995, *MNRAS* 273, 72
- White S. D. M., Navarro J. F. & Evrard A. E., 1993, *Nature* 366, 429
- Zabludoff A. I. & Mulchaey J. S., 1998, *ApJ* 496, 39 (ZM98)
- Zwicky F., 1933, *Helv. Phys. Acta* 6, 110

**Table 1.** X-ray data. Parameters refer to Eq. 9 ;  $n_{e0}$  is the central electron density. **Temperature error bars of clusters are computed from different reliable references (taking into account or not a cooling flow) as the maximum of two estimates : the dispersion among the measures and the quadratic mean of the quoted uncertainties (this procedure produces large uncertainty when there exists a possibility for strong temperature gradient).** They are given at a 90% confidence level, multiplying when necessary  $1\sigma$  errors by 1.64 (the errors of Fornax and RXJ1340.6 given by I96 and PA94, which confidence levels are not stated, are assumed to be  $1\sigma$ ).

(\*) Fornax and HCG62 have got a two-component gas density profile, the one in the second line corresponding to the nucleus. When no limiting radius  $R_{X\text{lim}}$  is given, we assumed  $R_{X\text{lim}}$  (Mpc)  $\simeq T_X/3$  (keV), a relation calibrated on other clusters.

name	$z$	$T_X$ (keV)	ref	$R_{X\text{lim}}$ (Mpc)	$\beta$	$r_{cX}$ (Mpc)	$n_{e0}$ ( $10^{-3}\text{ cm}^{-3}$ )	ref
A76	0.0416	$1.5^{+2.8}_{-0.9}$	D93		0.58	0.356	1.07	CNT97
A85	0.0518	$6.1 \pm 0.44$	MF98	1.4	0.497	0.06	6.5	P97
A119	0.0440	$5.62 \pm 0.61$	W00		0.56	0.378	1.18	CNT97
A401	0.0748	$8.3 \pm 1.16$	MF98	2.	0.606	0.285	4.31	BC96, EVB96
A426 (Perseus)	0.0183	$6.79 \pm 0.76$	F98	2.5	0.727	0.416	2.89	CK97
A576	0.0381	$4.02 \pm 0.31$	W00	1.5	0.64	0.24	2.47	MG96
A665	0.1816	$8.26 \pm 1.29$	D93	2.36	0.763	0.44	2.85	this study
A1060 (Hydra I)	0.0114	$3.1 \pm 0.14$	T96		0.61	0.094	5.00	LM96
A1377	0.0514	$2.6^{+0.7}_{-1.2}$	WJF97		0.46	0.188	0.75	CNT97
A1413	0.1427	$7.32 \pm 1.10$	W00		0.62	0.156	8.00	CNT97
A1656 (Coma)	0.0232	$8.11 \pm 0.79$	D93	4.	0.75	0.42	2.89	BHB92
A1689	0.1810	$9.23 \pm 1.05$	W00		0.72	0.205	14.0	CNT97
A1775	0.0696	$3.69 \pm 3.03$	W00		0.58	0.174	2.73	CNT97
A2029	0.0767	$8.7 \pm 0.75$	MF98	2.3	0.682	0.251	6.5	BC96, EVB96
A2052	0.0348	$3.03 \pm 0.23$	W00		0.67	0.142	4.43	CNT97
A2063	0.0337	$3.52 \pm 0.64$	W00		0.50	0.074	5.9	CNT97
A2163	0.201	$14.6 \pm 1.21$	EAB95	4.6	0.62	0.305	6.65	EAB95
A2199	0.0303	$4.27 \pm 0.28$	W00		0.62	0.117	6.5	CNT97
A2218	0.175	$6.84 \pm 2.83$	W00	2.1	0.71	0.276	5.54	SK96
A2256	0.058	$6.98 \pm 0.44$	W00	3.	0.795	0.54	2.51	HBN93
A2634	0.0312	$3.27 \pm 0.28$	W00		0.58	0.32	0.89	CNT97
A2657	0.0414	$3.81 \pm 0.40$	W00		0.52	0.124	4.4	CNT97
A2670	0.0745	$3.73 \pm 0.70$	W00		0.70	0.174	3.83	CNT97
AWM7	0.0176	$3.79 \pm 0.36$	W00	1.25	0.53	0.102	6.47	NB95
Hydra A (A780)	0.0522	$3.56 \pm 0.37$	W00	1.	0.7	0.145	6.5	D90
Fornax(*)	0.0046	$1.09 \pm 0.18$	I96	0.4	0.60	0.175	0.70	I96
					0.51	0.007	19.6	
HCG62(*)	0.0138	$0.96 \pm 0.07$	PB93	0.36	0.38	0.06	1.53	PB93
					0.9	0.019	15.6	
HCG94	0.04218	$2.75^{+0.9}_{-0.4}$	EMW95	1.	0.58	0.17	3.0	EMW95
NGC533	0.0172	$1.05^{+0.05}_{-0.09}$	MD96	0.58	0.69	0.237	0.7	MD96
NGC2300	0.0076	$0.97^{+0.11}_{-0.08}$	DM96	0.33	0.41	0.057	3.11	DM96
NGC4261	0.0088	$0.85^{+0.08}_{-0.16}$	DM95	0.6	0.31	0.026	2.9	DM95
NGC5044	0.0087	$0.98 \pm 0.04$	D94	0.4	0.53	0.028	7.9	D94
RXJ 1340.6+4018	0.171	$0.92 \pm 0.08$	PA94	0.4	1.	0.181	2.5	PA94

**Table 2.** Optical data. The first part corresponds to the galaxy spatial distribution and the second part to the luminosity function (Eq. 5).

(\*) TOP : type of optical profile : (1) stands for a King form (Eq. 2), (2) for a de Vaucouleurs form (Eq. 3), (3) for an integrated luminosity profile (Eq. 7) and (4) for a de Vaucouleurs projected luminosity density profile (cf Eq. 3).

(\*)  $\sigma_0$  : (1) and (2) : galaxies  $\text{Mpc}^{-2}$  ; (3) :  $L_0$  ( $10^{11} L_{\text{B}\odot}$ ) ; (4) :  $\sigma_{\text{L0}}$  ( $10^{11} L_{\text{B}\odot} \text{Mpc}^{-2}$ ).

(\*)  $r_c$  : for (2) and (4), corresponds to  $r_v$ .

(\*)  $\epsilon$  : for (2) and (4), corresponds to  $\gamma$ .

name	TOP <sup>(*)</sup>	$\sigma_0^{(*)}$	$r_c^{(*)}$ (Mpc)	$\epsilon^{(*)}$	$M_{\text{B lim}}$	ref	$M_{\text{B}}^*$	$\alpha$	ref
A76	(2)	39.8	0.485	0.678	-18.77	CNT97	-21.00	1.25	CNT97
A85	(1)	253	0.518	1	-17.76	M84	-21.17	1.13	OH89
A119	(2)	214	0.023	0.271	-19.77	CNT97	-20.98	1.25	CNT97
A401	(1)	165	0.4	1	-18.27	D78b	-20.96	1.25	D78a
A426	(1)	209	0.308	1	-17.34	KS83	-20.93	1.25	
A576	(1)	250	0.53	1	-16.26	MG96	-20.58	1.18	MG96
A665	(1)	168	0.5	1	-18.27	D78b	-20.21	1.25	D78a
A1060	(1)	228	0.180	1	-16.62	BO78	-20.93	1.25	
A1377	(2)	233	0.170	0.751	-19.47	CNT97	-21.00	1.25	CNT97
A1413	(2)	281	0.05	0.5	-19.97	CNT97	-20.59	1.25	CNT97
A1656	(1)	200	0.34	1	-18.25	KG82	-20.93	1.25	
A1689	(2)	140	0.059	0.43	-20.77	CNT97	-21.66	1.25	CNT97
A1775	(2)	205	0.007	0.227	-19.57	CNT97	-21.44	1.25	CNT97
A2029	(1)	198	0.35	1	-18.27	D78b	-21.14	1.17	OH89
A2052	(2)	175	0.105	0.553	-19.57	CNT97	-20.35	1.25	CNT97
A2063	(2)	153	0.19	0.767	-19.47	CNT97	-20.30	1.25	CNT97
A2163	(3)	139	0.532			SN97			
A2199	(2)	442	0.008	0.264	-19.27	CNT97	-20.17	1.25	CNT97
A2218	(1)	387	0.4	1	-18.27	D78b	-20.52	1.25	D78a
A2256	(1)	138	0.49	1	-18.27	D78b	-21.27	1.12	OHJ87
A2634	(2)	508	0.008	0.252	-19.27	CNT97	-19.75	1.25	CNT97
A2657	(2)	648	0.01	0.345	-19.57	CNT97	-20.86	1.25	CNT97
A2670	(2)	245	0.046	0.393	-19.47	CNT97	-21.00	1.25	CNT97
AWM7	(3)	6.25	0.102			B84			
Hydra A	(3)	6.07	0.146			D90			
Fornax	(1)	250	0.337	1	-13.20	F89	-20.82	1.32	FS88
HCG62	(3)	3.07	0.180			ZM98			
HCG94	(3)	7.72	0.17			HKA89, EMW95			
NGC533	(3)	2.64	0.140			ZM98			
NGC2300	(3)	3.26	0.245			G93			
NGC4261	(3)	5.82	0.163			N93			
NGC5044	(1)	331	0.188	1	-15.34	FS90	-20.93	1.25	
RXJ	(4)	3449	0.00524	0.665		PA94			

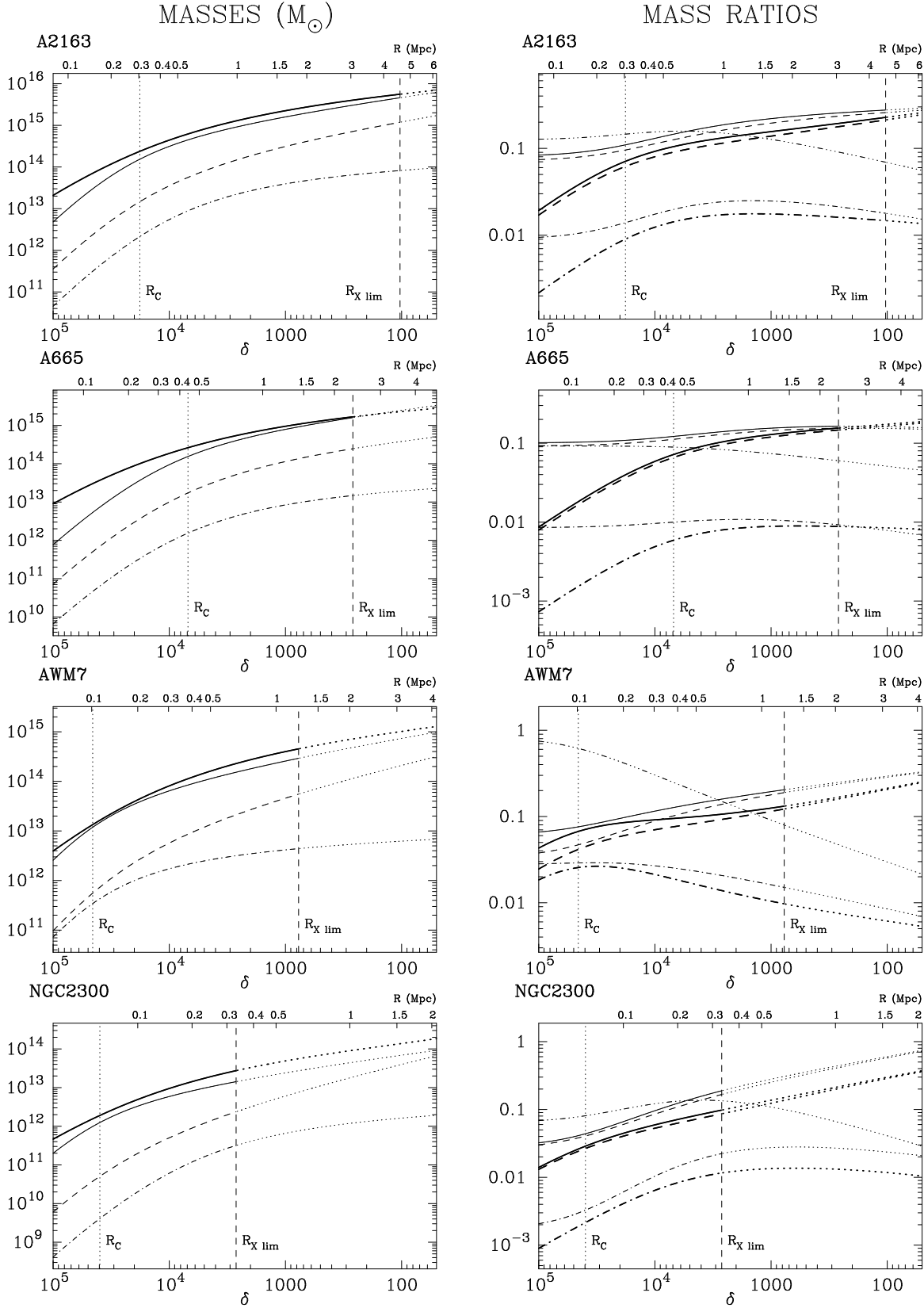


**Fig. 2.** Mass and mass ratio profiles for a few objects. The meaning of line styles is as follows : Left panels : thick line : SLM mass ; thin line : IHE mass ; dashes : gas mass ; dot-dashed line : stellar mass. Right panels : thick lines : baryon fraction (continuous), gas fraction (dashed) and stellar to total mass ratio (dot-dashed) in the SLM case (with EMN calibration) ; thin lines : same quantities for the IHE model ; three-dots-dash : stellar to gas mass ratio.

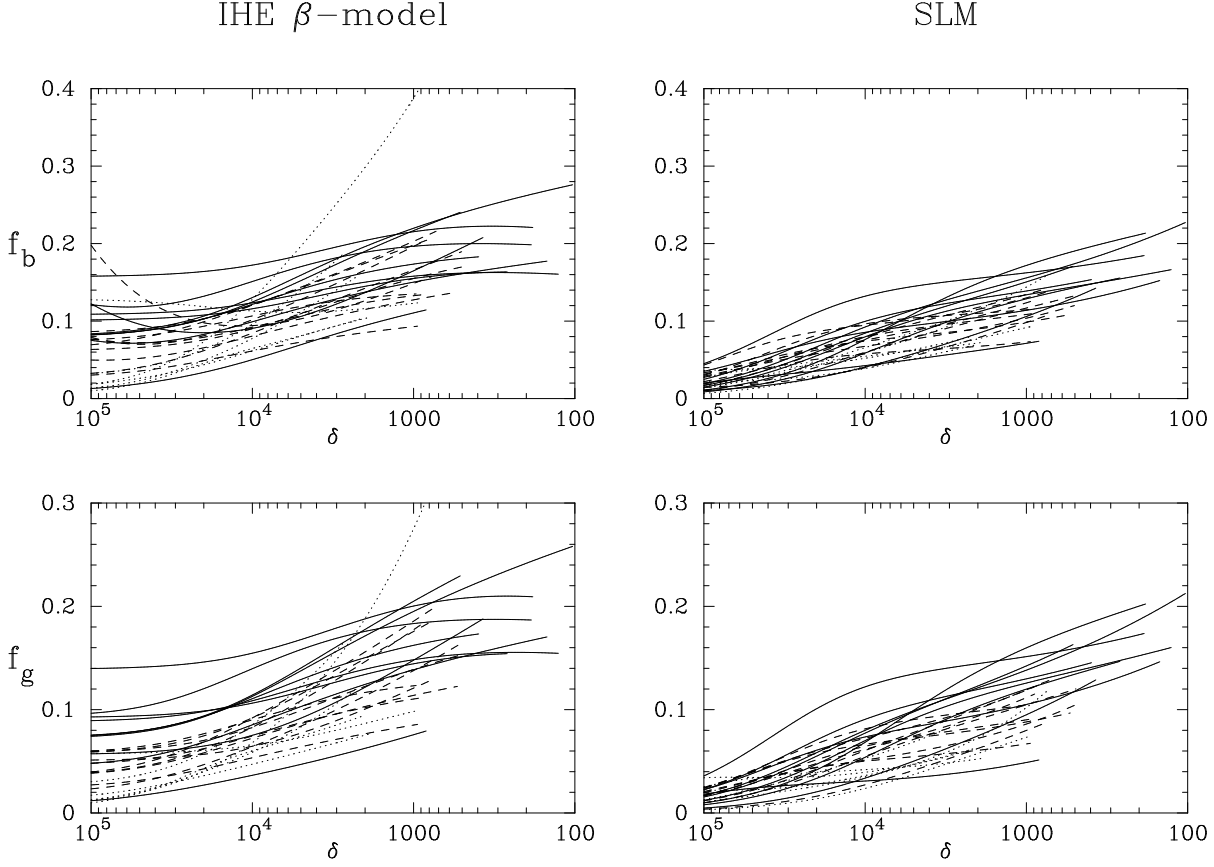


**Fig. 3.** Profiles of the baryon fraction and gas fraction as a function of mean overdensity for objects with the most reliable data. Left panels show these profiles in the case of the hydrostatic assumption and right panels for mass estimates derived from NFW's dark matter profile, with EMN normalisation. Groups ( $T_X \leq 2$  keV) are represented with dotted lines, cool clusters ( $T_X \leq 5$  keV) with dashed lines and hot clusters with continuous lines. The group with a very steeply rising baryon fraction in the IHE case has  $\beta = 0.31$ .

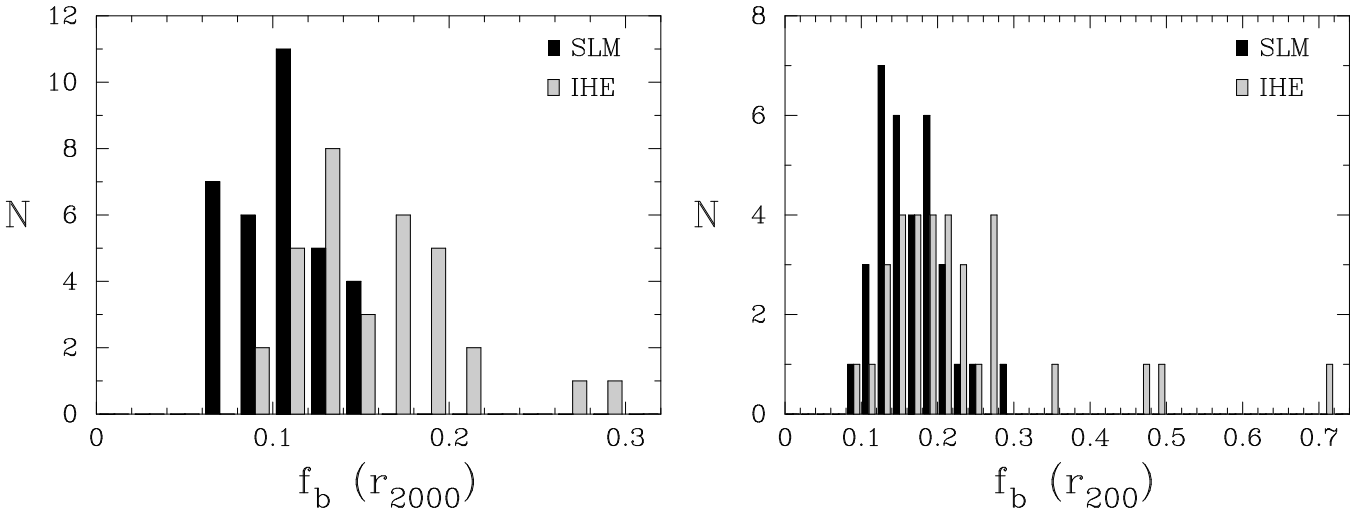


**Fig. 5.** Histogram of baryon fractions at  $r_{2000}$  and  $r_{200}$ , with IHE masses in grey and SLM masses in black. The object at  $f_b = 0.7$  is NGC 4261, which has the lowest X-ray slope  $\beta = 0.31$ .



**Table 3.** Dynamical quantities for the whole sample, at the limiting radius  $r_{200}$  and with the  $r_{500}-T_X$  normalization of EMN (the redshift is taken into account in this relation). The scalings with the Hubble constant are :  $M_{\text{tot}}$  and  $M_* \propto h_{50}^{-1}$ ,  $M_{\text{gas}} \propto h_{50}^{-\frac{5}{2}}$  and  $L \propto h_{50}^{-2}$ .

name	$r_{200}$ (Mpc)	$M_{\text{tot}}$	$M_{\text{gas}}$ ( $10^{13} M_{\odot}$ )	$M_*$	$f_b$ (%)	$M/L_B$ ( $M_{\odot}/L_{B\odot}$ )	$M_{\text{IHE}}/M_{\text{SLM}}$
A76	1.37	20.12	5.42	0.27	28.3	239	0.61
A85	2.72	129.70	10.21	2.90	10.1	143	0.70
A119	2.64	125.44	19.21	1.97	16.9	204	0.72
A401	3.07	225.02	44.32	1.56	20.4	462	0.75
A426	3.01	177.79	33.23	0.81	19.2	700	0.91
A576	2.25	75.29	10.74	0.99	15.6	243	0.84
A665	2.65	183.81	27.92	1.60	16.1	367	0.98
A1060	2.05	49.42	4.39	0.24	9.4	663	0.87
A1377	1.77	37.30	3.87	0.96	13.0	124	0.62
A1413	2.63	158.22	21.86	1.01	14.5	499	0.83
A1656	3.26	221.40	33.66	1.46	15.9	486	0.98
A1689	2.81	223.32	38.49	2.43	18.3	294	0.92
A1775	2.06	62.65	8.33	0.83	14.6	242	0.78
A2029	3.13	230.00	36.53	1.72	16.6	427	0.89
A2052	1.96	48.05	5.38	0.84	13.0	183	0.91
A2063	2.12	61.68	8.43	0.79	15.0	250	0.67
A2163	3.44	443.64	82.83	6.97	20.2	204	0.77
A2199	2.34	80.81	9.24	1.13	12.8	228	0.85
A2218	2.44	144.83	24.80	2.78	19.0	167	0.89
A2256	2.88	179.35	35.88	2.02	21.1	285	0.95
A2634	2.05	55.71	7.14	1.43	15.4	125	0.75
A2657	2.18	71.43	12.26	0.76	18.2	303	0.67
A2670	2.06	61.11	6.16	0.96	11.6	204	0.97
AWM7	2.25	73.61	13.05	0.56	18.5	423	0.68
Hydra A	2.07	59.78	7.38	0.46	13.1	420	0.95
Fornax	1.23	10.83	1.29	0.10	12.8	337	0.78
HCG62	1.14	9.34	1.50	0.15	17.6	196	0.50
HCG94	1.85	43.90	7.61	0.51	18.5	273	0.74
NGC533	1.18	10.01	1.10	0.15	12.5	207	0.91
NGC2300	1.16	10.33	2.31	0.13	23.7	249	0.49
NGC4261	1.08	8.68	1.92	0.30	25.6	93	0.36
NGC5044	1.16	8.98	0.81	0.17	10.9	171	0.74
RXJ	0.90	6.65	0.69	0.15	12.6	144	1.32

**Table 4.** Average dynamical quantities for the objects with the most reliable data (details on those that have been discarded can be found in the paragraph “notes on individual clusters”), using the EMN normalization. Values are given virial radius  $r_{200}$  (from SLM) but also at two other ones :  $r_{500}$ , the limiting radius within which EMN claim that the hydrostatic equilibrium is universally reached ;  $r_{2000}$  which we preferred to use because this represents the maximal extent of X-ray observations that is valid for the whole sample, including groups. Groups are defined by  $T_X < 2$  keV and hot clusters by  $T_X > 5$  keV.

		SLM (NFW’s DM profile)					IHE (hydrostatic equilibrium)			
		$f_{\text{gas}}$ (%)	$f_b$ (%)	$M_{\text{gas}}/M_*$	$M_{\text{tot}}/M_*$	$M/L_B$ ( $M_\odot/L_{B\odot}$ )	$f_{\text{gas}}$ (%)	$f_b$ (%)	$M_{\text{tot}}/M_*$	$M/L_B$ ( $M_\odot/L_{B\odot}$ )
all	at $r_{200}$	14.6	16.0	13.6	93.3	298	20.1	22.0	77.3	247
	at $r_{500}$	11.9	13.4	10.5	86.9	278	17.0	19.2	66.6	213
	at $r_{2000}$	8.9	10.4	7.7	84.5	270	12.8	15.2	60.9	195
groups	at $r_{200}$	14.7	16.5	9.0	62.4	200	26.6	29.8	45.7	146
	at $r_{500}$	11.0	13.1	6.3	58.3	186	19.7	23.4	39.0	125
	at $r_{2000}$	7.0	9.6	4.2	61.1	196	12.3	16.6	37.5	120
cool clusters	at $r_{200}$	13.4	14.6	12.2	95.0	304	17.2	18.8	77.8	249
	at $r_{500}$	11.0	12.3	9.3	88.6	283	15.0	16.7	67.9	217
	at $r_{2000}$	8.4	9.7	6.9	84.6	271	11.6	13.5	63.2	202
hot clusters	at $r_{200}$	15.9	17.0	19.4	118.1	378	18.8	20.2	104.3	334
	at $r_{500}$	13.7	14.8	15.7	109.8	351	17.3	18.9	89.1	285
	at $r_{2000}$	10.7	11.9	11.8	104.8	335	14.4	16.0	78.5	251

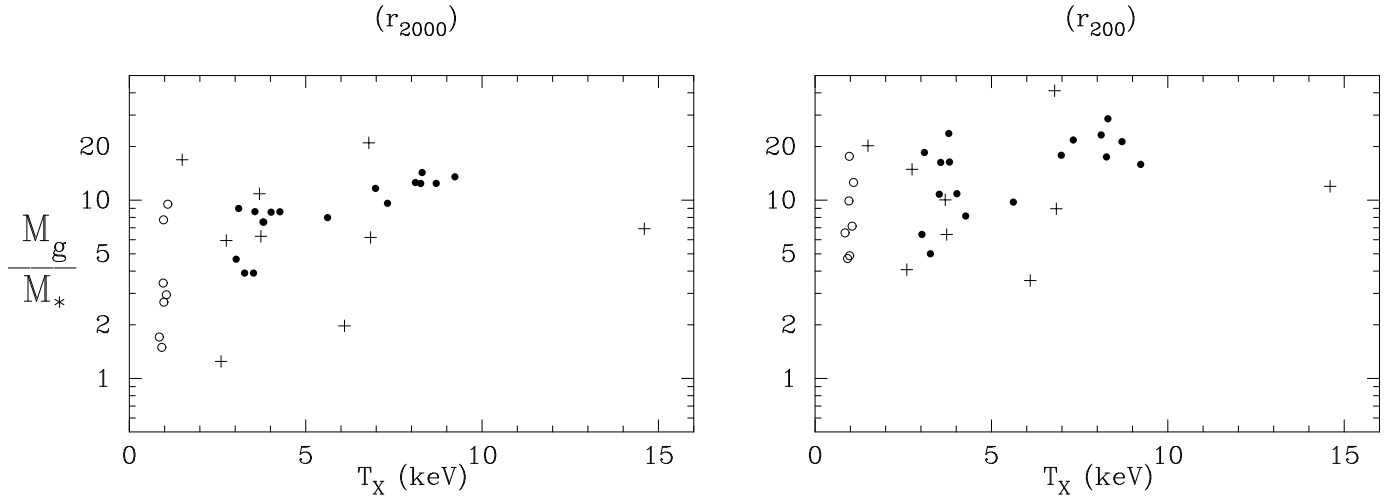


**Fig. 6.** Gas to galaxy mass ratio versus X-ray temperature. Open circles are for groups, filled circles are for clusters, and crosses refer to poor quality optical or gas masses.

**Table 5.** Same as Table 3 but with the  $r_{200}$ – $T_X$  normalization of BN.

name	$r_{200}$ (Mpc)	$M_{\text{tot}}$	$M_{\text{gas}}$ ( $10^{13} M_{\odot}$ )	$M_*$	$f_b$ (%)	$M/L_B$ ( $M_{\odot}/L_{B\odot}$ )	$M_{\text{IHE}}/M_{\text{SLM}}$
A76	1.52	26.47	6.40	0.31	25.4	272	0.52
A85	3.02	174.74	11.97	3.11	8.6	180	0.58
A119	2.93	167.47	22.42	2.27	14.7	236	0.60
A401	3.41	297.72	50.75	1.65	17.6	577	0.63
A426	3.34	234.89	37.20	0.86	16.2	879	0.77
A576	2.50	100.32	12.21	1.07	13.2	299	0.70
A665	2.95	244.16	31.16	1.72	13.5	455	0.83
A1060	2.28	66.58	4.99	0.25	7.9	852	0.72
A1377	1.97	50.07	4.63	0.99	11.2	162	0.52
A1413	2.92	211.20	24.82	1.04	12.2	650	0.69
A1656	3.62	294.04	37.42	1.53	13.2	615	0.82
A1689	3.12	295.02	42.65	2.61	15.3	362	0.78
A1775	2.29	83.81	9.59	0.96	12.6	278	0.64
A2029	3.48	305.31	40.92	1.82	14.0	537	0.75
A2052	2.18	64.21	6.04	0.89	10.8	230	0.76
A2063	2.35	82.53	9.89	0.81	13.0	328	0.56
A2163	3.82	586.39	94.45	7.42	17.4	253	0.65
A2199	2.60	108.21	10.48	1.28	10.9	270	0.70
A2218	2.71	191.28	27.75	2.97	16.1	206	0.75
A2256	3.20	235.80	39.93	2.15	17.8	350	0.81
A2634	2.28	74.50	8.31	1.64	13.4	146	0.63
A2657	2.42	95.12	14.32	0.80	15.9	378	0.56
A2670	2.28	81.87	6.87	1.06	9.7	248	0.80
AWM7	2.50	97.92	15.18	0.58	16.1	542	0.57
Hydra A	2.30	79.83	8.21	0.48	10.9	537	0.79
Fornax	1.37	14.52	1.49	0.11	11.0	414	0.65
HCG62	1.26	12.51	1.82	0.16	15.8	246	0.41
HCG94	2.05	58.31	8.77	0.54	16.0	345	0.62
NGC533	1.32	13.41	1.25	0.16	10.6	263	0.76
NGC2300	1.28	13.73	2.79	0.14	21.4	308	0.41
NGC4261	1.20	11.55	2.39	0.32	23.4	117	0.30
NGC5044	1.29	12.07	0.94	0.18	9.3	216	0.61
RXJ	1.00	8.85	0.74	0.15	10.0	194	1.11

**Table 6.** Same as Table 4, but using the BN normalization.

		SLM (NFW's DM profile)					IHE (hydrostatic equilibrium)			
		$f_{\text{gas}}$ (%)	$f_{\text{b}}$ (%)	$M_{\text{gas}}/M_*$	$M_{\text{tot}}/M_*$	$M/L_{\text{B}}$ ( $M_{\odot}/L_{\text{B}\odot}$ )	$f_{\text{gas}}$ (%)	$f_{\text{b}}$ (%)	$M_{\text{tot}}/M_*$	$M/L_{\text{B}}$ ( $M_{\odot}/L_{\text{B}\odot}$ )
all	at $r_{200}$	12.6	13.7	14.6	117.1	375	21.0	22.8	81.1	260
	at $r_{500}$	10.3	11.5	11.2	107.5	344	17.7	19.8	68.8	220
	at $r_{2000}$	7.7	9.0	8.0	100.8	323	13.4	15.8	60.9	195
groups	at $r_{200}$	13.1	14.5	9.9	78.4	251	28.8	31.8	48.2	154
	at $r_{500}$	9.7	11.4	6.8	72.1	231	21.2	24.8	40.3	129
	at $r_{2000}$	6.3	8.3	4.4	71.7	230	13.2	17.4	36.8	118
cool clusters	at $r_{200}$	11.5	12.5	13.1	119.7	383	17.7	19.3	81.4	260
	at $r_{500}$	9.4	10.5	9.9	110.0	352	15.5	17.3	69.9	224
	at $r_{2000}$	7.3	8.4	7.1	101.7	325	12.1	14.0	63.1	202
hot clusters	at $r_{200}$	13.5	14.4	20.6	147.7	473	19.1	20.5	109.5	350
	at $r_{500}$	11.7	12.6	16.5	135.5	434	17.7	19.2	92.2	295
	at $r_{2000}$	9.3	10.3	12.3	125.2	401	14.9	16.5	79.2	253

IHE  $\beta$ -model

SLM

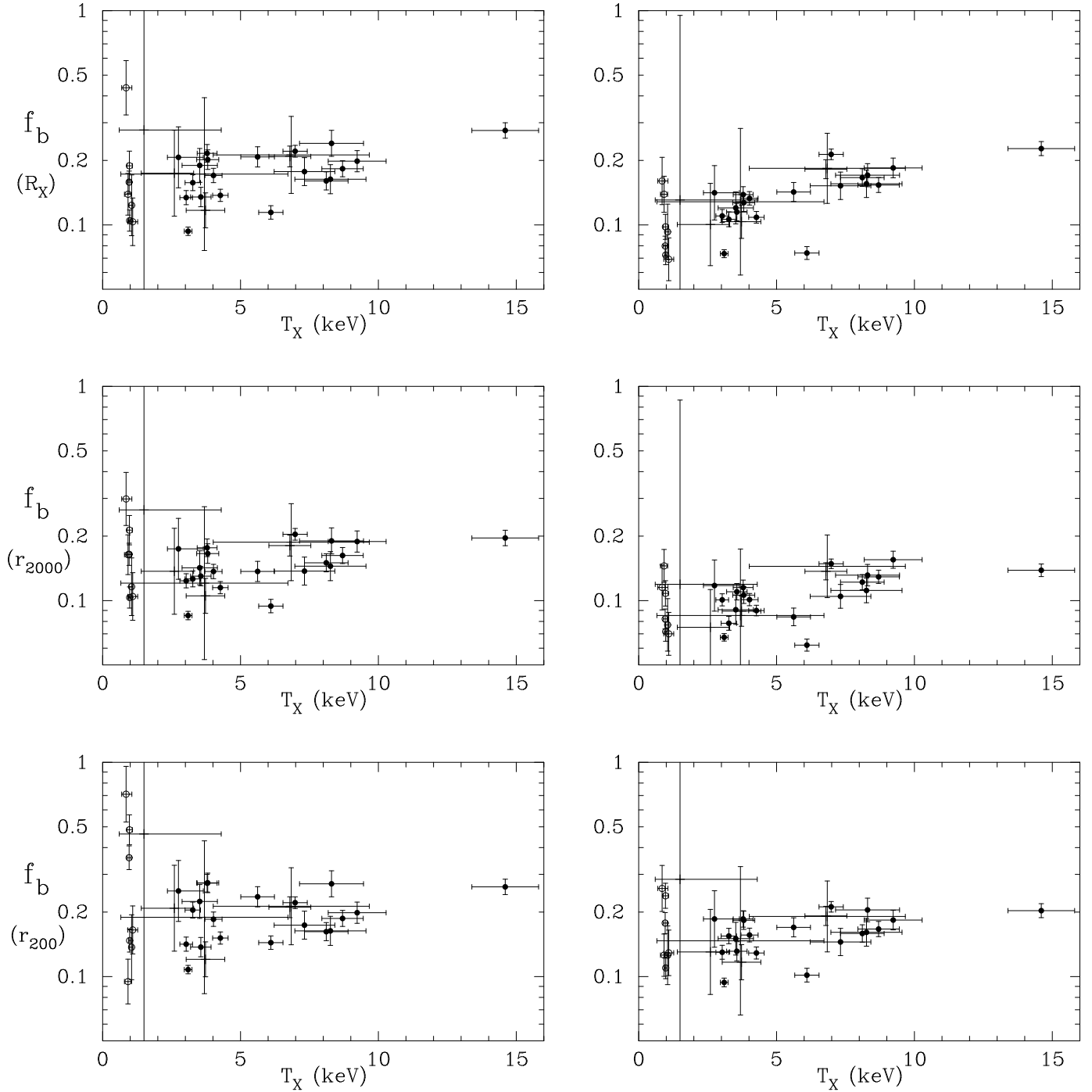


**Fig. 7.** Baryon fractions in the sample as a function of X-ray temperature. Top : at  $R_{X \text{ lim}}$ . Middle : at  $r_{2000}$ . Bottom : at  $r_{200}$ . Left : hydrostatic masses. Right : SLM masses. Groups are shown as open circles and objects with poor quality temperature measurements (and therefore masses) as crosses.

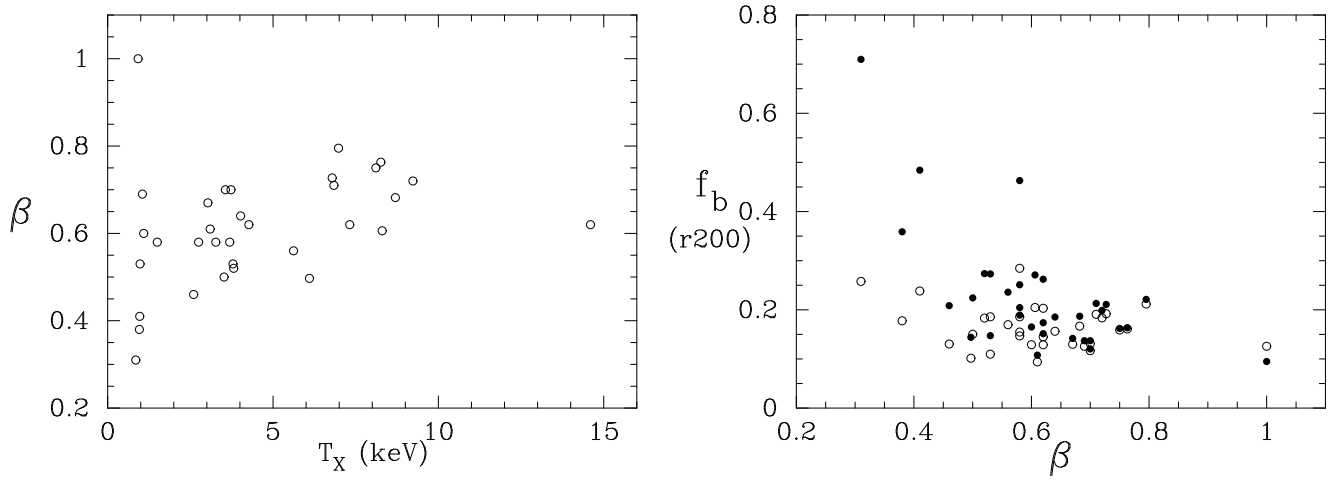


**Fig. 8.** The slope  $\beta$  derived from the best-fit of a  $\beta$ -model to X-ray images plotted versus the temperature. On the *right panel* is plotted the baryon fraction (at  $r_{200}$ ) in the IHE  $\beta$ -model (filled symbols) compared to the SLM (open symbols) as a function of  $\beta$ .